The International Journal of Advanced Manufacturing Technology (2019) 101:881–900
https://doi.org/10.1007/s00170-018-2936-3

ORIGINAL ARTICLE

Process robustness and strength analysis of multi-layered dissimilar joints using ultrasonic metal welding

Abhishek Das[1] · Iain Masters[1] · David Williams[1]

Received: 23 June 2018 / Accepted: 23 October 2018 / Published online: 9 November 2018

Abstract

This paper investigates the effects of process parameters on the joint strength and process robustness when multi-layered joints of dissimilar metals are produced by ultrasonic metal welding (UMW). Three layers of 0.3-mm aluminium sheet are welded with a single 1.0-mm copper sheet which is representative of electric vehicle battery interconnects. A process robustness study in which welding pressure, amplitude of vibration and welding time are varied to produce satisfactory welds is reported. The weld quality is evaluated by performing lap shear and T-peel tests where maximum loads are considered as the quality indicator. Response surfaces are developed to identify the relationship and sensitivity between the input process parameters and output quality indicators. A feasible weldability zone is defined for the first time by identifying the under-weld, good-weld and over-weld conditions based on load-displacement curves and corresponding failure modes. Relying on the weldability zone and response surfaces, multi-objective optimisation is performed to obtain maximum lap shear and T-peel strength which resulted in Pareto frontier or trade-off curve between both objectives. An optimal joint is selected from the Pareto front which is verified and validated by performing confirmation experiments, and further, used for T-peel strength analysis of different interfaces of the multi-layered joint. To conclude, this paper determines both the optimal weld parameters and the robust operating range.

Keywords Ultrasonic metal welding · Automotive battery interconnects · Joint strength · Process robustness · Response surface methodology · Feasible weldability zone

1 Introduction

Ultrasonic metal welding (UMW) is an effective welding process for both similar and dissimilar materials [1, 2], especially for thin material [3, 4] in various industrial applications including electronics, electrical, automotive [5–7], and aerospace [8] industries. In comparison with fusion welding processes, UMW succeeds on joining highly conductive and reflective materials having multiple stack-ups of varying thicknesses by avoiding brittle intermetallic formation [5]. Fusion welding processes, such as laser welding, pulsed arc welding or resistance spot welding also have quality concerns including spatter, porosity, heat-affected zone or burn-through [9–11]. Moreover, they often need shielding gas to produce good quality joint. UMW being a solid state process does not require consumables or suffer from the any aforesaid quality issues as the maximum process temperature is normally only 0.3 to 0.5 times that of the absolute melting temperature of the substrate materials [12, 13]. Furthermore, the UMW technique is suitable for soft materials such as aluminium (Al), nickel (Ni), copper (Cu), gold (Au) and silver (Ag) [1, 14]. UMW is, however, not suitable for hard (e.g. ferrous alloys) and thick materials (> 3 mm) although a few diverse combinations like Al-to-steel, metal-to-ceramic or metal-to-glass are reported in literature [15, 16]. In recent years, there has been a growing interest in dissimilar metal and alloy joining as a result of diverse joining requirements including electric vehicle battery tab-to-busbar interconnects, automotive body-in-white lightweight structure or electronics component fabrication. Several attempts have been made using electron beam welding [17], resistance spot welding [18], laser welding [19, 20], self-pierce riveting [21, 22], friction stir welding [23, 24] and ultrasonic metal welding [1, 4] to join dissimilar materials using a single lap configuration. However, little work has been

✉ Abhishek Das
A.Das.1@warwick.ac.uk

[1] WMG, The University of Warwick, Coventry CV4 8GJ, UK

Table 1 Test materials used for experimental investigation

Type	Material	Specification	Chemical composition (wt%)	Thickness [mm]
Tab	Aluminium (Al)	AW1050A-H18; BS EN546	Si < 0.25, Fe < 0.40, Cu < 0.05, Mn < 0.05, Mg < 0.05, Zn < 0.07, Ti < 0.05, Al-balance 99.50	0.3
Busbar	Copper (Cu)	CW004A-H065; BS EN1652 (C101HH; BS 2870)	Cu > 99.99, O < 0.0005, other-balance	1.0

conducted on dissimilar metal joining of multi-layered aluminium to copper using ultrasonic metal welding.

Recent advancement in high energy and high power batteries has made them the main alternative power source for electric vehicles (EVs), hybrid or plug-in hybrid electric vehicles (HEVs or PHEVs) [25, 26]. Typically, a battery pack using hundreds, even thousands, of individual cells based on lithium-ion (Li-ion) electrochemistry, connected in series and/or parallel to deliver the required power and capacity [13], is becoming the standard. Increasing uptake of such vehicles in the market place requires development and improvement of battery pack manufacturing methods. Electrically conductive materials such as copper, aluminium and nickel are extensively used in automotive Li-ion batteries for making electrodes, current collectors or busbars [27]. Making of dissimilar materials joining is essential, such as multiple Al tabs to Cu busbar in a pouch cell–based battery pack. Large joint areas and excellent joint strength are also required to support high power application as automotive vehicles are often exposed to adverse thermal and impulse conditions [7]. Making these tab joints involves several challenges, including joining of thin multiple stack-ups of dissimilar materials, highly conductive and reflective surfaces, mechanical/vibrational or thermal damage during joining, and joint durability [13]. Hence, there is a need for suitable joining techniques to support the diverse joining requirements of battery pack manufacture. Due to solid state nature of UMW, this is suitable for joining multiple layer stack-ups.

Fundamental research on the effects of input parameters on weld quality, process robustness, and joint strength analysis are necessary for successful evaluation of UMW for multi-layered dissimilar materials joining. Kong et al. [28] used an ultrasonic consolidation method to join aluminium alloy in a single lap configuration to evaluate peel strength. Elangovan et al. [2] used a similar approach to study the joining of similar material with varying weld parameters and optimise 0.2 mm thick Cu-to-Cu

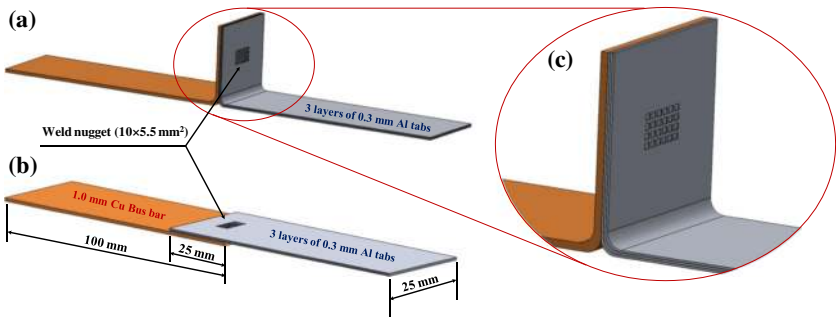

Fig. 1 A pictorial example of ultrasonic welding to produce tabs-to-busbar interconnect. **a** T-peel specimen, **b** lap shear specimen and **c** enhanced view of T-peel (1.0 mm Cu busbar to 0.3 × 3 layers of Al tab)

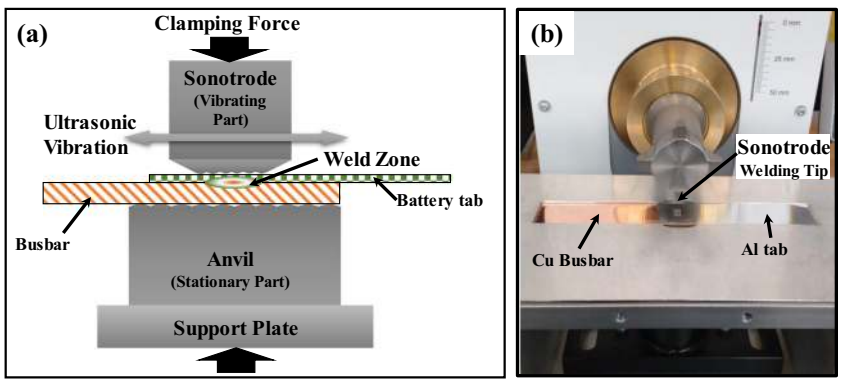

Fig. 2 Ultrasonic metal welding **a** illustration of welding principle, and **b** tab-to-busbar joining set-up

Table 2 Full factorial experimental design—factors and levels

Factor	Levels			
Welding pressure, p [bar]	1	2	3	4
Amplitude, a [μm]	40	45	50	55
Welding time, t [sec]	0.15	0.30	0.45	0.60

joints using a design of experiments. They identified the influence of process parameters on the weld quality when a single layer lap configuration was used, and further, they reported maximum weld strength at 2 bar welding pressure, 2.25 s welding time and 50 μm amplitude of vibration. The effects of welding pressure and welding time on single lap ultrasonic welding were demonstrated by Kim et al. [4] where they welded a 0.2-mm copper (Cu) sheet to a 0.2-mm nickel plated copper (Cu[Ni]) sheet and sensitivity of process parameters were reported. Attempts have also been made to weld Al/Mg/Al tri-layered clad sheets together [29]. A few studies have been conducted on dissimilar material-based single lap joints to find the effects of weld parameters on the microstructure and mechanical performances using various metal and alloy combinations as diverse as Al-to-Cu [30, 31], Al-to-steel [1, 32], Mg-to-Al [33], Al-to-Ti [34] and Cu-to-Mg [35]. However, limited work has been conducted on multi-layer ultrasonic welded joints to identify the robust process parameters and corresponding tensile strength. A layer-by-layer additive manufacturing application has been investigated where 3000 series Al foils are deposited one by one using ultrasonic consolidation methods [36]. Further, dynamic stress analysis, vibrational energy loss or simulations for understanding the ultrasonic welding considering multiple layers were reported in literature [37–40]. Despite these studies which have been conducted on UMW, to understand its fundamental behaviours, there exists a lack of quality guidelines for implementing the UMW into volume production for joining multi-layers of dissimilar materials. Furthermore, the sensitivity of process robustness and weld quality to process parameters are limited in the literature and must be established.

To establish UMW quality and robust process parameter ranges for multi-layer dissimilar material joints, this paper focuses on an experimental investigation based on three layers of Al welded with a single Cu sheet. The influencing process parameters investigated were clamping pressure, welding time and amplitude of ultrasonic vibration [2, 4]. These process parameters are selected as input variables in a full factorial experimental design. Lap shear and T-peel strengths are used as response variables and maximum load for both cases is used to analyse the sensitivity to input variables. Using the maximum loads from the lap shear and T-peel tests, response surfaces are estimated which explains weld quality distribution and sensitivity of the responses. Furthermore, a feasible weldability zone is defined for the first time for UMW process using multi-layer dissimilar materials.

This paper is arranged as follows: Section 2 outlines the investigated material properties, full factorial experimental design and sample preparation. Section 3 develops the response surface methodology–based models to explain the effects of process parameters on lap shear and T-peel loads, and subsequently, optimisation. Final conclusions are drawn in Section 4.

Table 3 Constant parameters during joining of tabs-to-busbar using ultrasonic metal welding

Parameter	Value
Ultrasonic frequency	20 kHz
Peak-to-peak amplitude	60 μm
Holding time after welding	0.3 s
Joining area	10×5 mm^2

2 Experimental details

2.1 Investigated materials

Copper and aluminium are the most commonly used materials for electric vehicle battery interconnects. Pouch

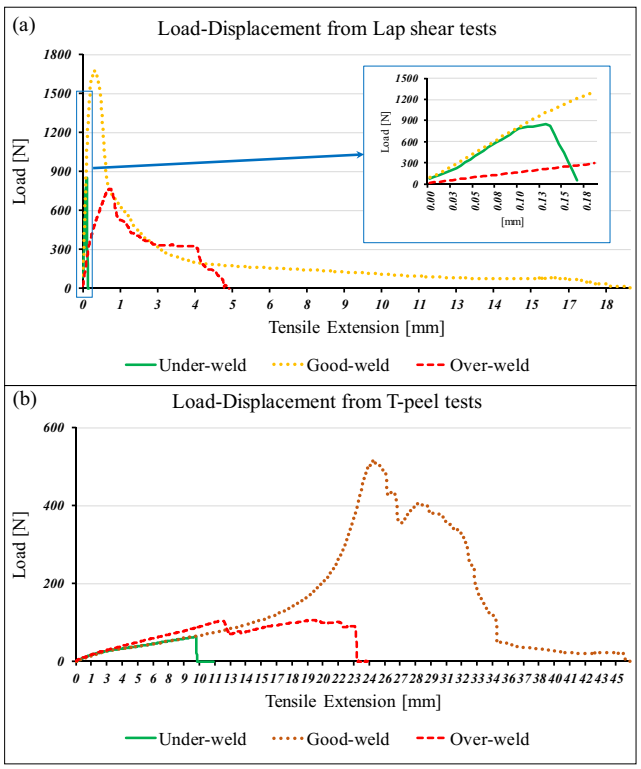

Fig. 3 Typical load-displacement graphs for the under-weld (e.g. at p = 1 bar, a = 45 μm and t = 0.15 s), good-weld (e.g. at p = 1 bar, a = 55 μm and t = 0.45 s), and over-weld (e.g. at p = 4 bar, a = 55 μm and t = 0.60 s) conditions from **a** lap shear tests (inset showing enhanced view of the lap shear tests of under-weld joint) and **b** T-peel tests

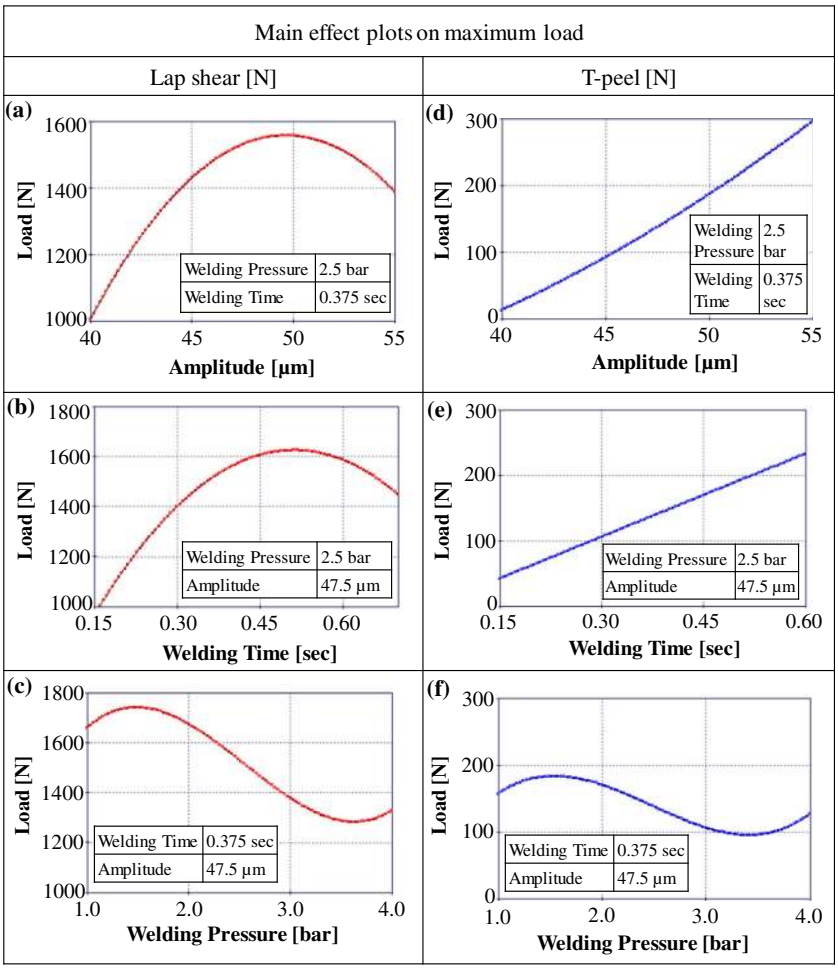

Fig. 4 Main effect plots of input process parameters on the maximum lap shear and T-peel loads

cells are used by two EV pioneers, GM (Chevrolet volt, bolt and Spark) and Nissan (Leaf), with copper busbar material and aluminium tab material [41, 42]. The main joining method for tab-to-busbar connections is UMW. In this experimental investigation, 1.0-mm thick copper (Cu) was used to represent busbar and 0.3-mm aluminium (Al) for the tabs. Details of test materials used for the experimental investigation are summarised in Table 1. The test samples were prepared in both lap shear and T-peel configurations where the busbar was kept as lower part with the tab sheets applied on the top. A schematic of tabs-to-busbar test specimens is illustrated in Fig. 1. Three layers of aluminium tab of 0.3 mm were welded with 1-mm thick copper busbar to produce an industrial representative joint configuration. For example, GM's Chevrolet Volt battery tab welding configuration with three aluminium battery tabs to busbar was produced [42]. Both busbar and tab dimensions are 100 mm in length by 25 mm in width with 25 mm overlap where the weld was placed carefully for the lap shear samples [1, 43]. Further, the welding specimens conform to the standard weld coupon geometry as shown in Fig. 1.

2.2 Experimental set-up and design

A schematic of ultrasonic metal welding process and a picture of the welding set-up are shown in Fig. 2. UMW works under a clamping pressure when high frequency ultrasonic vibration, typically 20 kHz or above, is applied to join substrate materials by creating solid state bonds [44]. In principle, high-frequency vibration creates progressive shearing and plastic deformation between the mating surfaces which breaks the oxide/contamination and produces an atomic bond at elevated temperature (i.e., typically at 0.3 to 0.5 times the absolute melting temperature of the substrate materials) [12, 13]. Several researchers proposed different joining mechanisms [4] including localised heating and plastic deformation [45, 46], mechanical interfacial interlocking [36, 47], and chemical bond involving diffusion [48].

In this study, the ultrasonic welding was performed using Telsonic MPX ultrasonic welder having 6.5 kW maximum power and 5 kN maximum force. The maximum amplitude (i.e. peak-to-peak amplitude) for the ultrasonic vibration was 60 µm and the trigger mode time was set at 0.2 s which allowed converting of the traversing pressure to welding

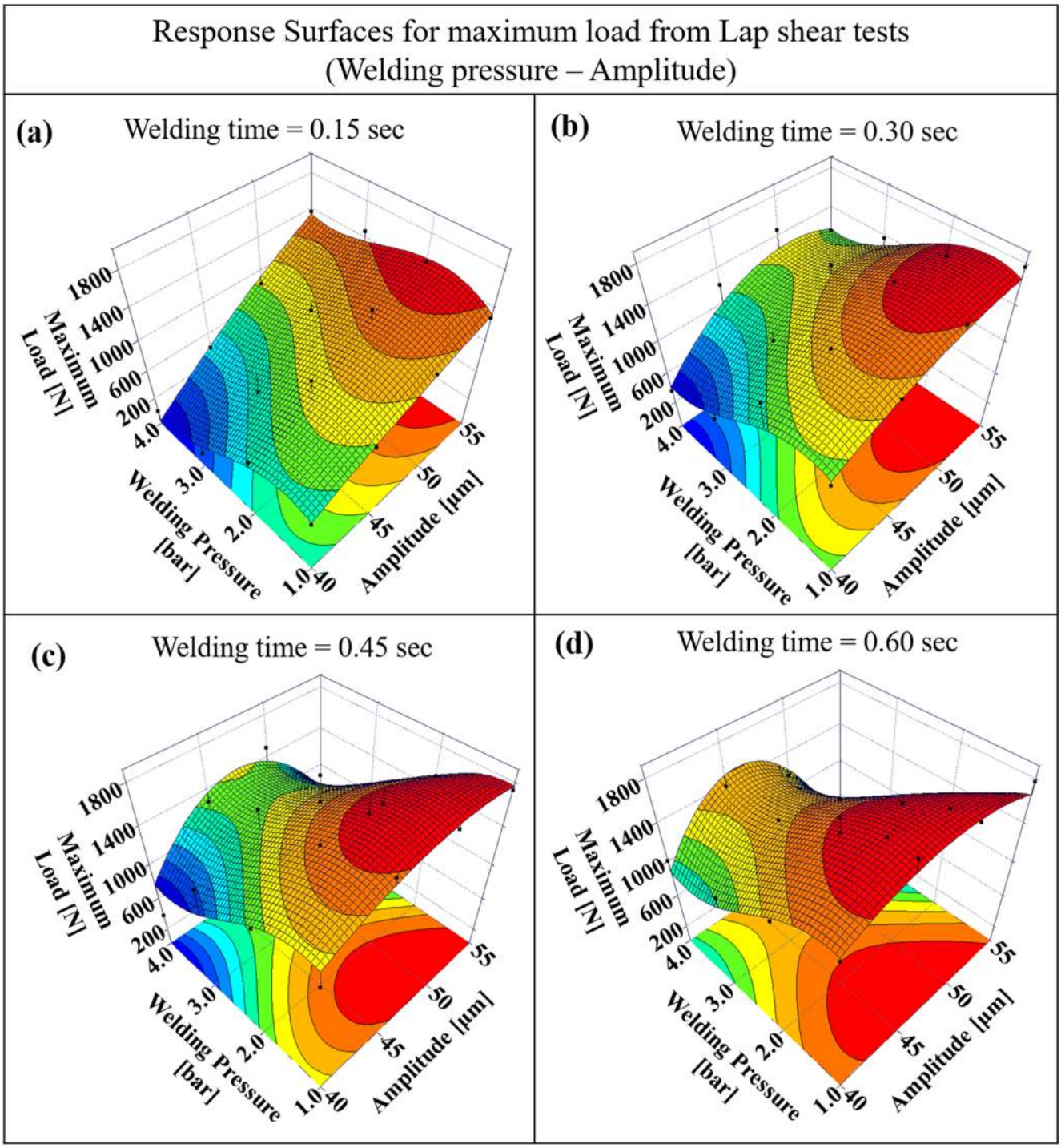

Fig. 5 Welding pressure and amplitude responses presented at various levels of welding time in **a** to **d** showing the complex behaviour on the maximum lap shear loads

pressure. The sonotrode used for this application can create ultrasonic welds of 10×5 mm^2 area. Three process parameters: welding pressure, welding time and amplitude of ultrasonic vibration were selected as input design variables. The output variables chosen to represent weld quality were the maximum loads obtained from the lap shear and T-peel tests, as described in Section 2.3. A full factorial design was used to establish the relation between the input and output parameters. In general, full factorial design provides experimental data at each possible combination of factors and their corresponding levels which leads to more powerful conclusions by reducing the error [49, 50]. Initial screening tests

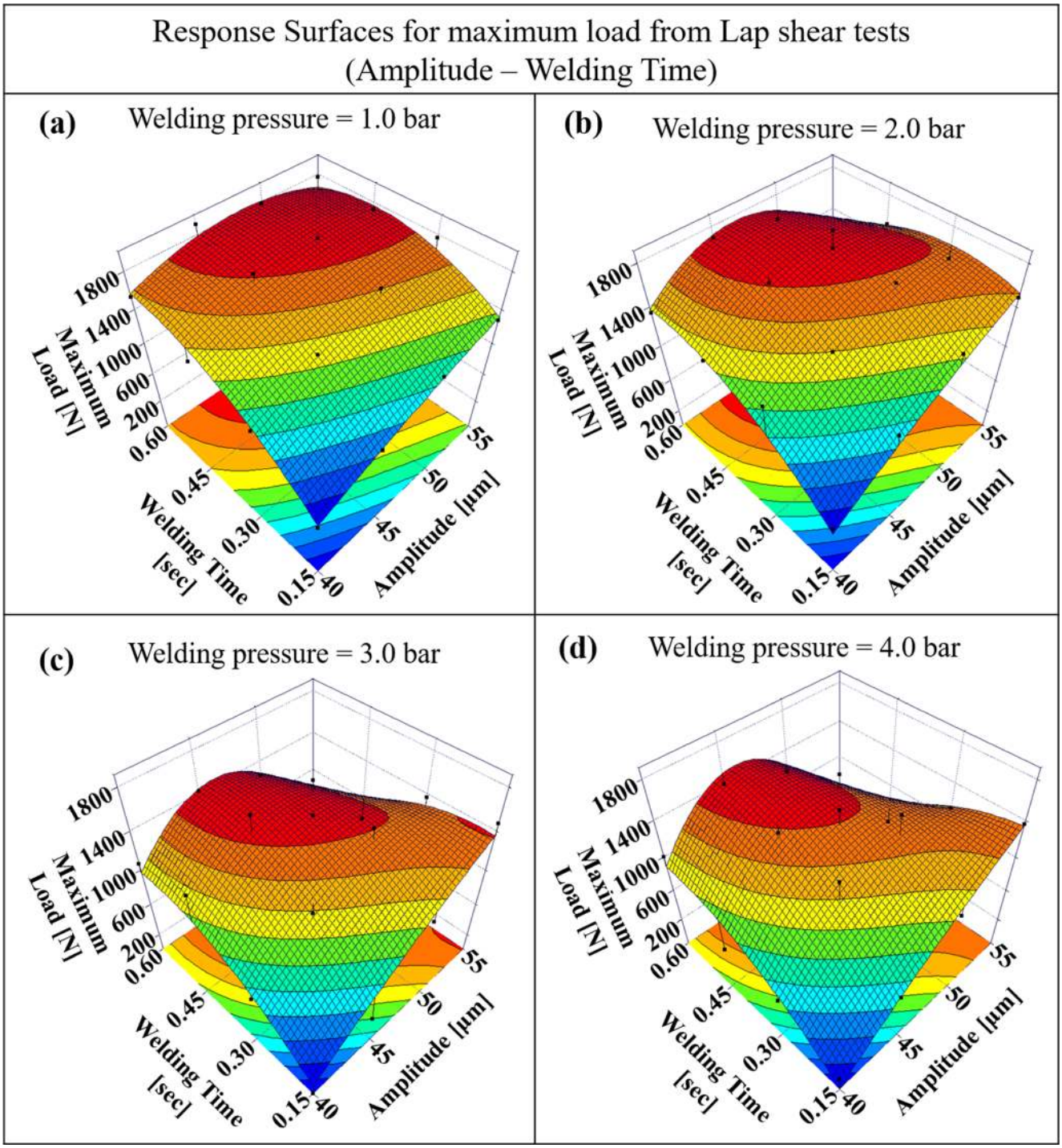

Fig. 6 Amplitude and welding time responses presented at various levels of welding pressure in **a** to **d** showing the complex behaviour on the maximum lap shear loads

were conducted prior to selecting the process parameter ranges. Relying on the pilot screening results, the welding pressure, amplitude and welding time were varied in four levels. Table 2 lists all input factors with their levels. A 0.3-s holding time was applied after performing the welding. Table 3 summarises the constant parameters used for welding the various experimental design conditions. As three factors were varied at four levels using a full factorial design, the number of experimental conditions was 64 with 8 replicates (i.e. 4 replicates for lap shear and 4 replicates for T-peel). A total of 512 test samples were prepared for the lap shear and T-peel tests.

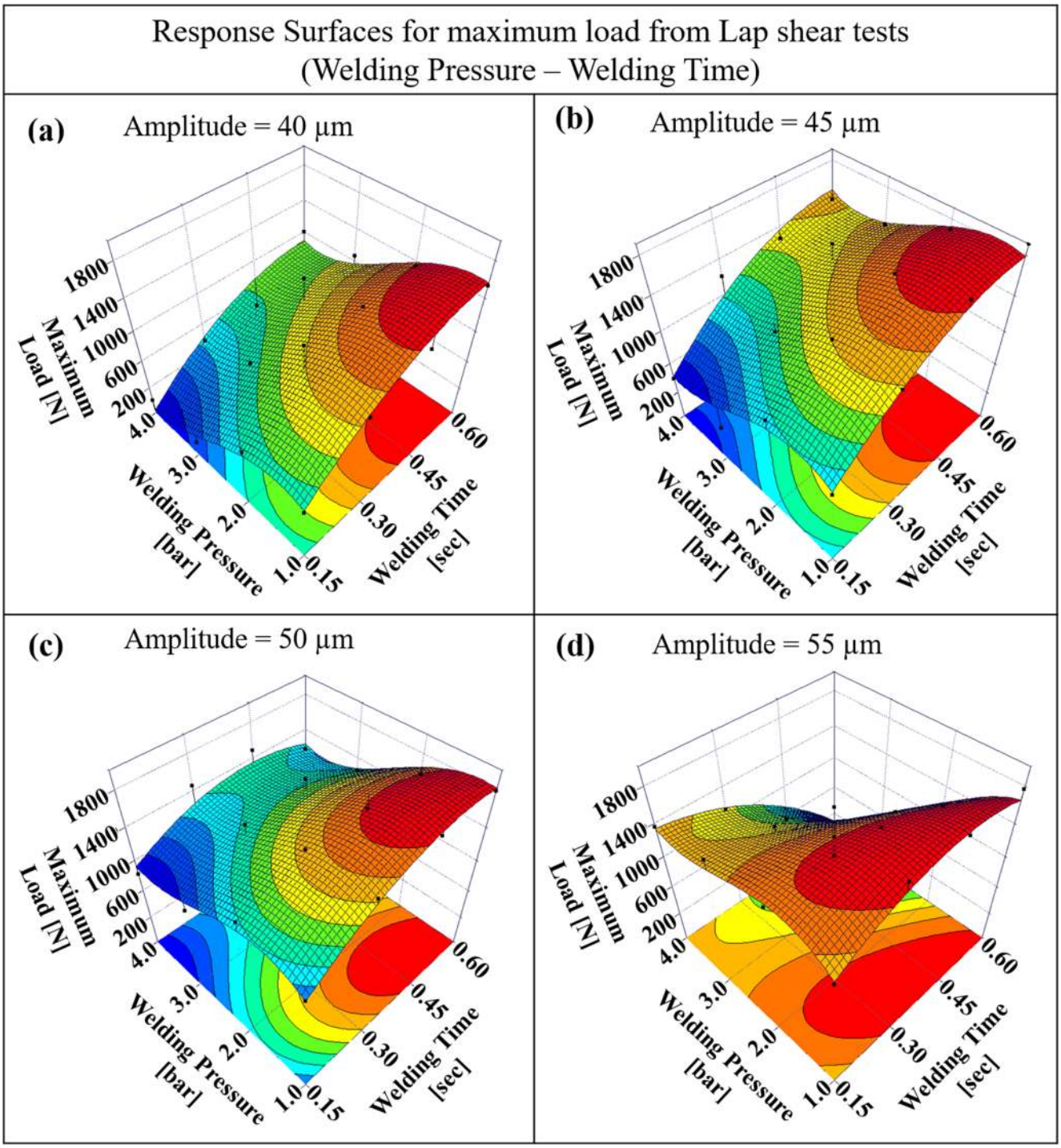

Fig. 7 Welding pressure and welding time responses presented at various levels of amplitude in **a** to **d** showing the complex behaviour on the maximum lap shear loads

2.3 Lap shear and T-peel tests

The weld quality was evaluated using the maximum loads obtained from lap shear and T-peel tests. Each test variant was replicated four times and the average was used for analyses. Lap shear and T-peel tests were carried out using an Instron 5800 test frame with a 100-kN load capacity. After the welding, the T-peel test samples were prepared by bending the tabs and busbar 90° in opposite directions to allow specimens to be gripped (see Fig. 1). Lap shear and T-peel tests were performed using cross head speeds of 2 mm/min and 10 mm/min, respectively.

In Fig. 3, load-displacement behaviours obtained from lap shear and T-peel tests are plotted where three

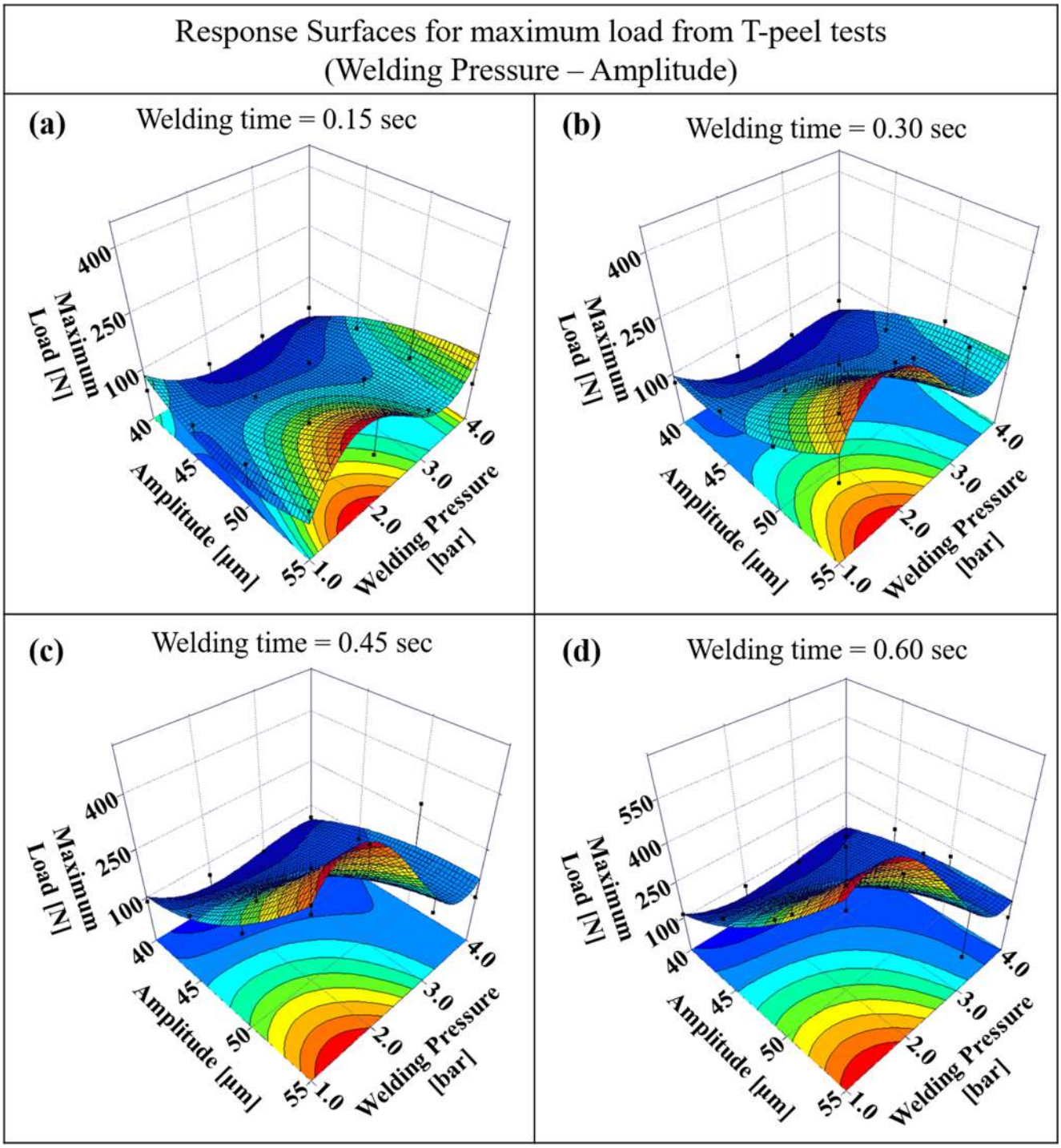

Fig. 8 Welding pressure and amplitude responses presented at various levels of welding time in **a** to **d** showing the complex behaviour on the maximum T-peel loads

weld conditions: under-weld, good-weld and over-weld can be visualised. Typically, a good/normal-weld exhibits two stages: first, the load reaches the peak load after which the Al tab material starts to tear while the weld nugget area remains intact with the lower part, and then the load drops to form a sloping plateau before the two pieces were completely separated. This indicates strong material adhesion in between the aluminium tabs and copper busbar. In under-weld, joints fail within the first region of the good-weld and do not reach the peak value. This indicates a weak bond and results in clear interfacial separation of Al tabs from the Cu busbar.

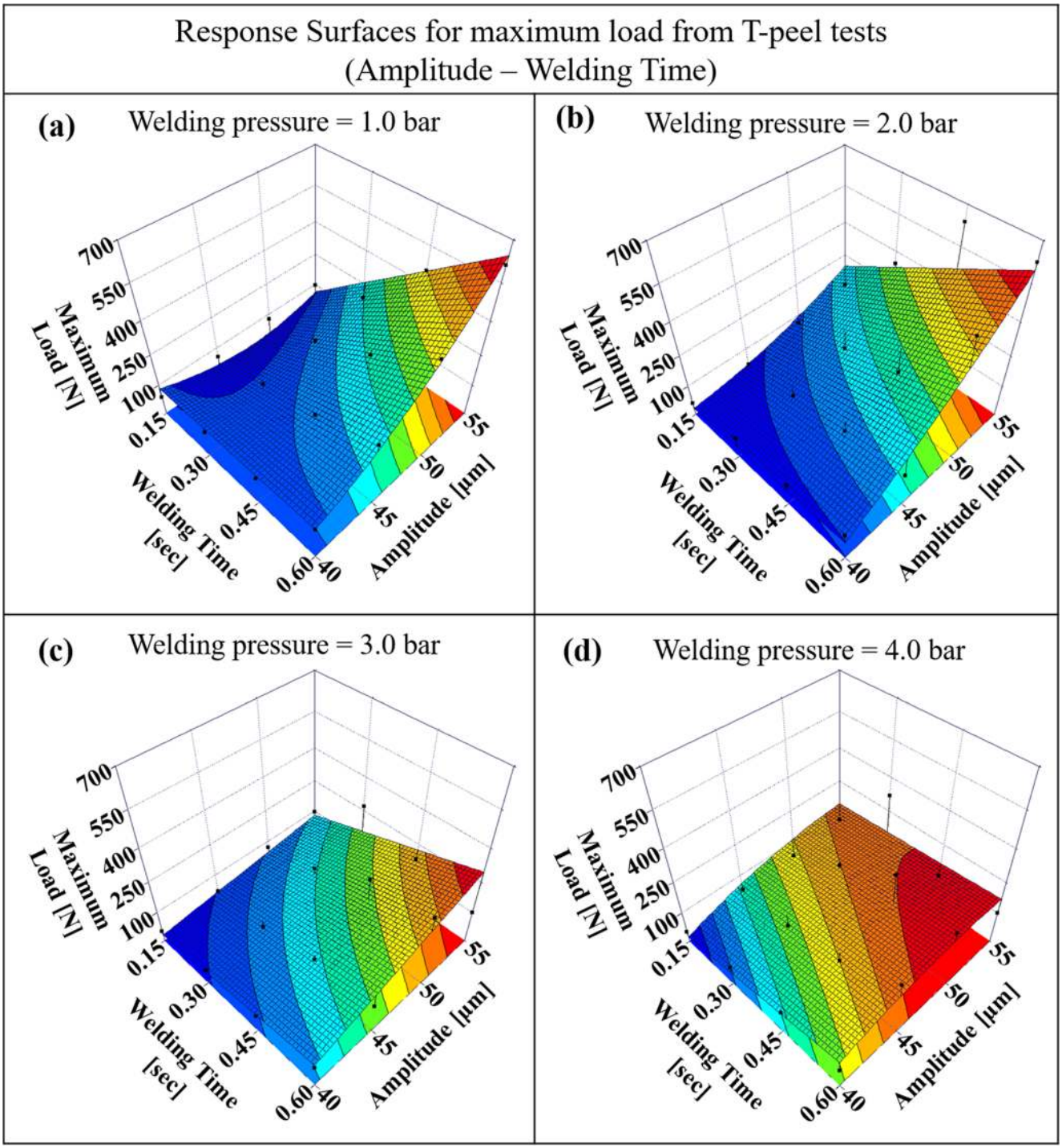

Fig. 9 Amplitude and welding pressure responses presented at various levels of welding time in **a** to **d** showing the complex behaviour on the maximum T-peel loads

The inset in Fig. 3 shows an enhanced view of the under-weld lap shear test where the weld experienced a lower peak load at low tensile extension. Similarly, in 'over-weld' condition, the joint exhibited early material failure by tearing due to cracks developing around the weld nugget which resulted in a much lower peak load and lower tensile extension compared to good-weld. Partial/full circumferential fracture with tear was observed for over-weld test specimens along with early separation of tabs from the busbar. Therefore, based on load-displacement graphs and failure modes, this paper utilises the maximum lap shear and T-peel loads as indicators for ultrasonic weld quality.

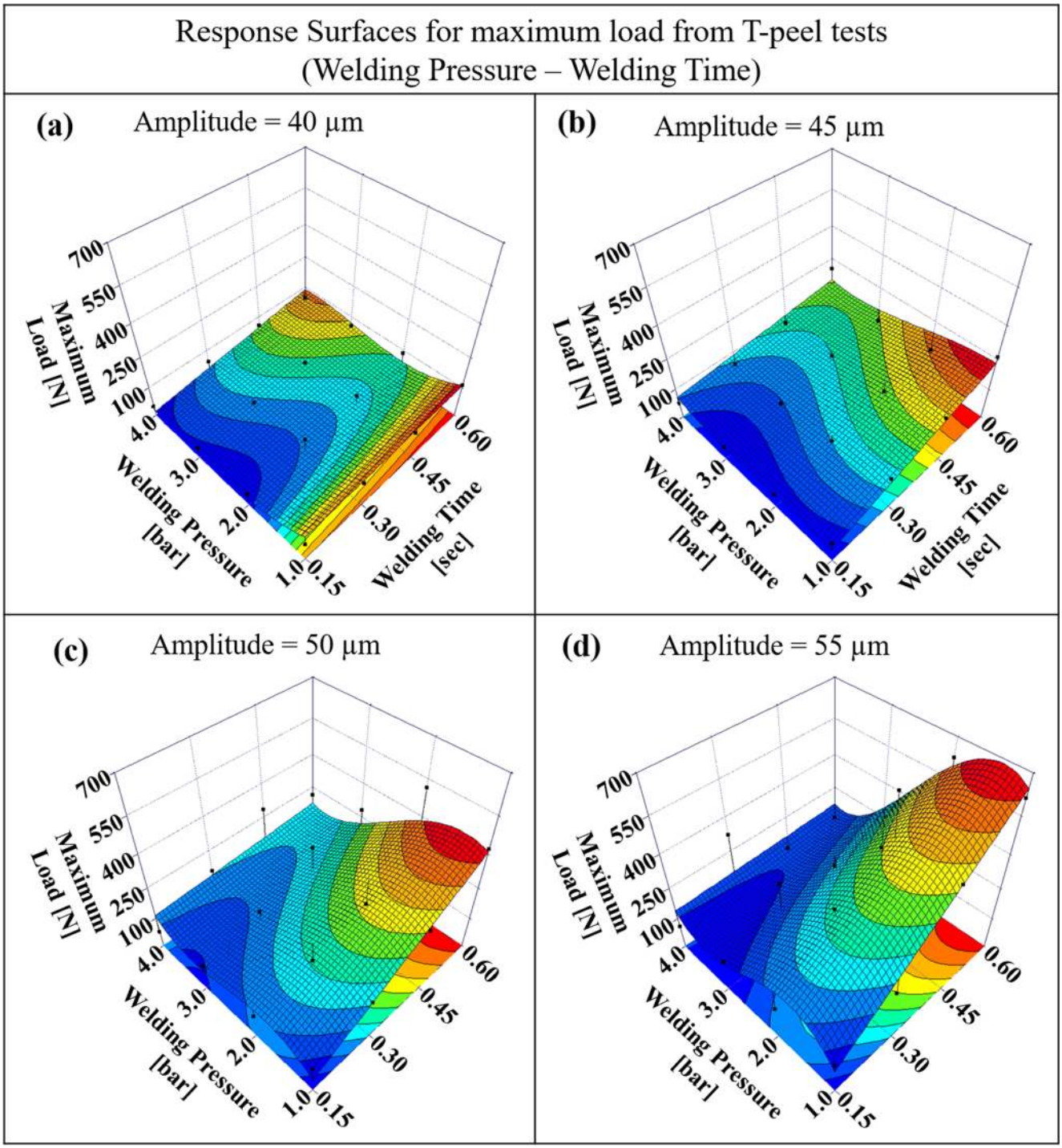

Fig. 10 Welding pressure and welding time responses presented at various levels of welding time in **a** to **d** showing the complex behaviour on the maximum T-peel loads

3 Results and discussions

3.1 Response surfaces for the maximum lap shear and T-peel loads

After carrying out the experimental runs as per the full factorial design with four levels (refer to Table 2), the maximum lap shear and T-peel loads were used to evaluate process robustness and joint strength. To visualise the effects of input process parameters on output variables, the response surface technique was adopted. Several methods have been developed to construct accurate response surface models [51, 52]. A stepwise polynomial regression model was selected to keep the

Table 4 Weld quality classification based on lap shear and T-peel failure modes and load-displacement characteristics

Quality class	Failure mode	Detailed description
Under-weld	Interfacial separation with no or partial adhesion	• Low to medium lap shear and T-peel loads and low tensile extension at failure • Weld failure inside the weld nuggets with no or partial adhesion of materials (i.e. tab and busbar materials are completely separated or partial adhesion of tabs with the busbar) • No significant deformation in the weld nugget and no cracking around the perimeter.
Good-weld	Partial interfacial separation with tear	• Comparatively medium to high lap shear and T-peel loads and larger grip displacement till complete separation of upper and lower parts • Leaving partial or full materials attached in the nugget area with tab material tear • Ultrasonic nugget impression with low deformation in the weld nugget and no cracking around the perimeter
Over-weld	Partial or full circumferential fracture with or without tear	• Medium to low lap shear and T-peel loads • Larger grip displacement compared to under-weld condition but lower than good-weld • Weld failure starts around the perimeter due to cracks around the weld nugget • Partial material tear or full nugget fracture with no tear

regression models tractable, yet with a good predictive ability (i.e. a compromise between over-fitting and under-fitting). In stepwise regression, the model is updated with one predictor at a time (which is either added or removed), after all predictors have been accounted for, the one with the best F-test value is chosen. In this study, the model terms were selected based on the best F-test value in accordance with the significance levels where the thresholds for addition or removing a term were 0.05 and 0.1, respectively. In general, narrower process window and fewer levels of experimental factors are suitable for second-order regression model [4]. Fujita, Kounoe [53] explained that second-order regression model does not account for enough variation in the data points when they are obtained from wide experimental window with large variations, resulting in poor local estimates of the studied variables [4]. Thereafter, the maximum lap shear and T-peel loads were expressed in third-order polynomial regression equations as shown in Eqs. (1) and (2), respectively. F_{LS} and F_{TP} represent the estimated maximum lap shear and T-peel loads using input process parameters, i.e. welding pressure (p), amplitude (a) and welding time (t). The coefficient of determination for lap shear regression equation was 0.93 which adequately explained the lap shear response. Similarly, the coefficient of determination obtained from the T-peel regression was 0.86 which was slightly lower than the lap shear, yet enough to explain the welding process in terms of T-peel strength.

$$F_{LS} = -5106.14 + 140.46a + 3250.69p + 14276.73t - 1.11a^2 - 86.76ap - 784.92p^2 - 314.37at - 18898.69pt - 5026.56t^2 + 1.22a^2p + 92.93p^3 + 3.15a^2t + 835.08apt + 191.74p^2t - 9.65a^2pt \quad (1)$$

$$F_{TP} = 8177.34 - 268.60a - 6643.90p - 4533.87t + 1.85a^2 + 179.38ap + 2051.73p^2 + 113.50at + 1325.53pt - 0.61a^2p - 47.42ap^2 - 255.68p^3 - 31.56apt + 5.95ap^3 \quad (2)$$

The main effects of individual process parameter on the maximum lap shear and T-peel loads are plotted in Fig. 4. The maximum lap shear strength initially increased when both amplitude and welding time increased. After reaching an optimal point, the lap shear strength started decreasing. This can be attributed to higher welding energy concentration due to increasing amplitude and welding time. Therefore, incremental increases in both amplitude and welding time shifted the lap shear strength from under-weld to good-weld and subsequently reached maximum lap shear strength. However, further increase in both input variables causes deformation in the upper tabs due to excessive ultrasonic vibration and energy input to the weld nugget. As a result, weld quality started shifting towards the over-weld condition indicated by the reduction in lap shear strength. T-peel strength was observed to increase almost linearly with amplitude and welding time when the other input variables were held constant at their mid-range values (i.e. welding pressure and welding time were kept at 2.5 bar and 0.375 s respectively when amplitude was varied). Similarly, amplitude and welding pressure were kept at 47.5 μm and 2.5 bar when welding time was varied. In contrast, both the maximum lap shear and T-peel loads exhibited non-linear, decreasing trend when the welding pressure was increased. Higher welding pressure is associated with increased heat generation due to greater sliding resistance [1], leading to reduced freedom to propagate microbonding or interfacial locking between welding surfaces as the joining parts are more firmly held together. Therefore, higher welding pressure resulted in a weak weld nugget or sometimes

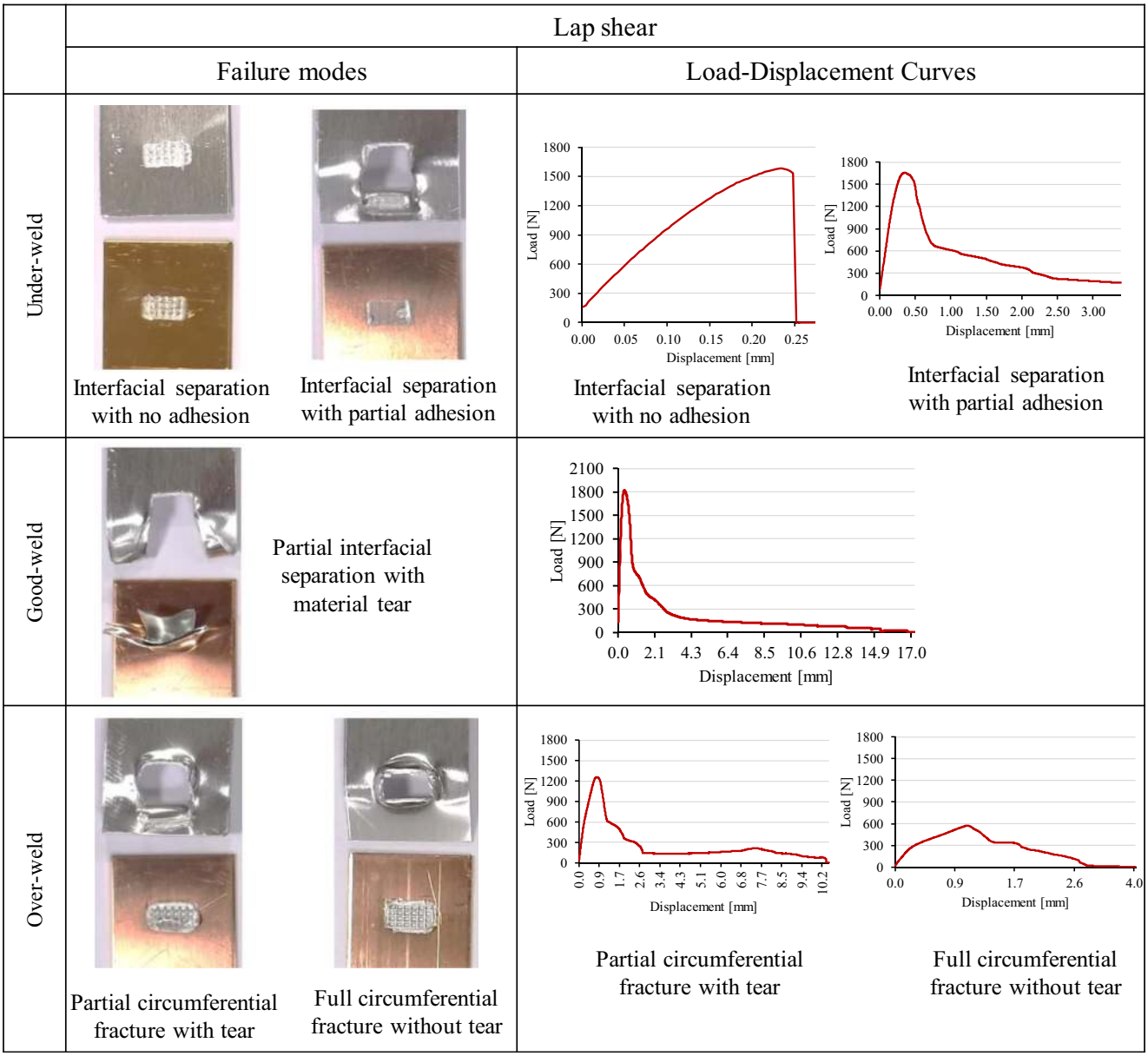

Fig. 11 Failure modes and load-displacement curves from lap shear tests with weld quality

developed crack around the weld when amplitude and welding time were set at higher levels [4].

The response surfaces for maximum lap shear and T-peel loads with respect to welding pressure, amplitude and welding time are shown in Figs. 5, 6, 7, 8, 9 and 10, which illustrate the complex non-linear behaviour of input process parameters. Further, the zoned and contoured floor of the individual 3D response surface demonstrates the sensitivity of the input process parameters to the output responses.

In case of maximum lap shear load, the welding pressure and amplitude responses are presented at various levels of welding time as shown in Fig. 5(a–d). It can be seen that for all values of welding time at low welding pressure, the rate of change in lap shear load is higher at lower welding time and gradually decreases with larger welding time as the welding quality moved from under-weld to good-weld. In contrast, at higher welding pressure, amplitude and welding time, over-welds were obtained as excessive energy input increased the welding temperature at the interface and resulted in material thinning, cracking of tabs etc. The response surfaces as a result of amplitude and welding time variation at different levels of welding pressure are plotted in Fig. 6(a–d). From these plots, it can be observed that the maximum lap shear strength gradually decreases with higher values of welding pressure, and furthermore, shifted towards the mid values of amplitude as the combination of higher welding pressure, welding time and amplitude produced over-weld. The welding pressure and welding time responses for different levels of amplitude are in Fig. 7(a–

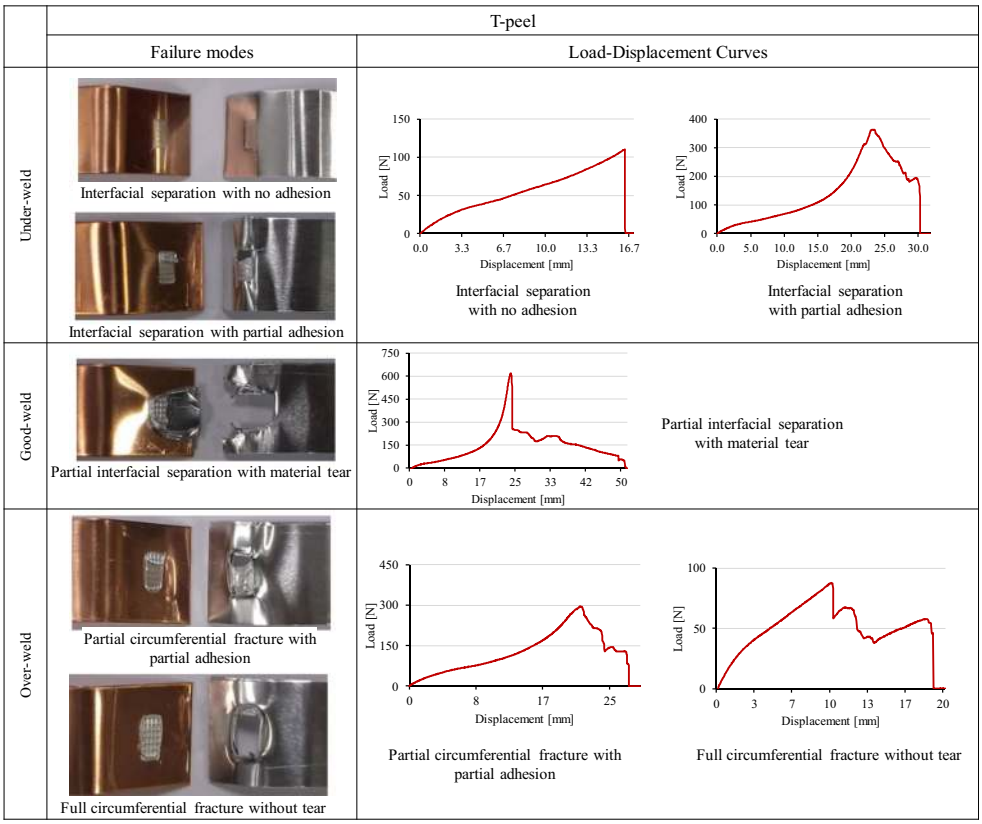

Fig. 12 Failure modes and load-displacement curves from T-peel tests with weld quality

d). From these responses, it can be observed that combination of lower values of welding pressure and higher values of welding time produces good-welds with high lap shear strength; however, both increasing welding pressure and welding time gradually generate over-welded joints. Similar to lap shear plots, the response surface plots for welding time and amplitude at various levels of welding time are presented in Fig. 8(a–d) which illustrates the complex behaviour of the maximum T-peel load. It can be noted from these response surface plots that the region to obtain high T-peel strength remains the same for the combination of welding pressure and amplitude; however, gradually shifted upwards with increase in welding time. As shown in Fig. 9(a–d), increasing both amplitude and welding time increases the T-peel strength although the effect is reduced with increasing welding pressure moving towards the over-weld condition. The response plots for welding pressure and welding time at different levels of amplitude are given in Fig. 10(a–d) with gradual incremental increase observed.

It is evident from the response surfaces and corresponding contour plots that maximum lap shear strength could be achieved around 50 μm amplitude (range: 50–55 μm), 0.45 s welding time (range: 0.45–0.60 s), and 1.5 bar welding pressure (range: 1–2 bar). Similarly, maximum T-peel strength could be obtained around 55 μm amplitude (range: 50–55 μm), 0.60 s welding time (range: 0.45–0.60 s), and 1.5 bar welding pressure (range: 1–2 bar).

3.2 Failure-based weld quality classification

In spite of being a good indicator of weld quality, the maximum lap shear and T-peel loads do not effectively distinguish between the three classes of weld: under-weld, good-weld or over-weld indicated in Fig. 3. Therefore, failure modes in combination with maximum lap shear and T-peel loads have been used to define weld quality classification as summarised in Table 4.

A visual representation of under-weld, good-weld and over-weld conditions in terms of their failure modes and load-displacement curves obtained from lap shear and T-peel tests, respectively, are shown in Figs. 11 and 12. Under-weld joints are characterised by interfacial separation with no/partial adhesion of materials and no cracks around the weld nugget. From the both lap shear and T-peel tests, it was observed that Al tabs are fully separated or having partial adhesion with the Cu busbar. In case of *good-weld*, limited interfacial separation was observed in association with material tearing and maximum area of the weld nugget remained attached after the tests. Under these conditions, large loads were obtained from the both lap shear and T-peel tests. The over-weld joints were observed when partial or full circumferential fracture was observed around the perimeter of the weld nugget. Often partial circumferential fracture occurred with material tearing and partial adhesion in the weld nugget, i.e. Al tabs

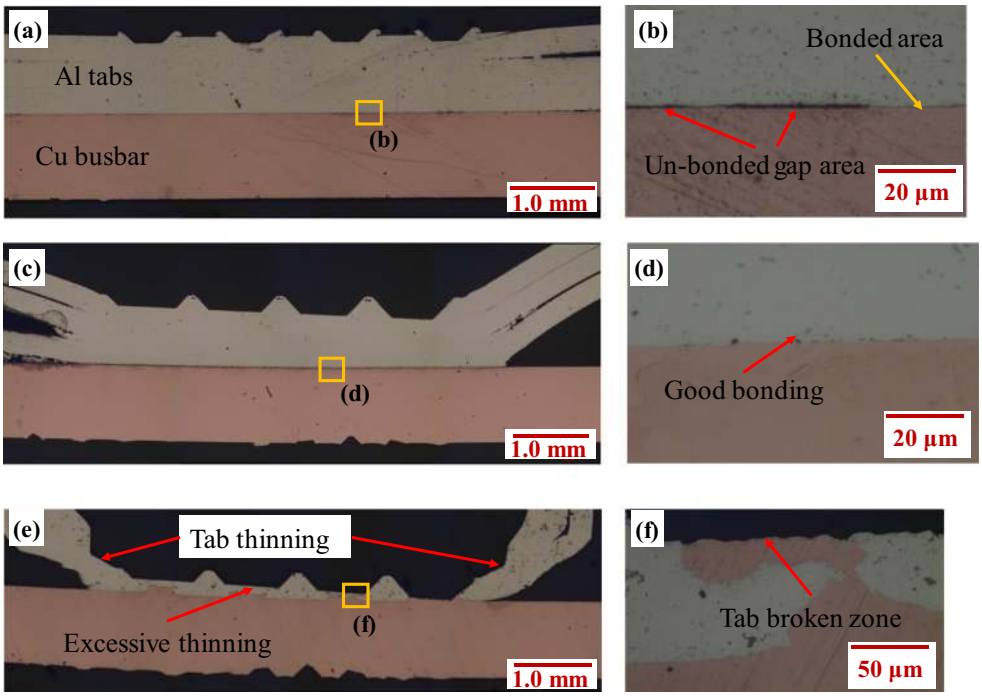

Fig. 13 Optical images of weld cross-sections obtained from **a** under-weld (e.g. at $p = 1$ bar, $a = 45$ µm and $t = 0.15$ s) condition; **b** enhanced joint area showing the un-bonded gap area of under-weld; **c** good-weld (e.g. at $p = 1$ bar, $a = 55$ µm and $t = 0.45$ s) condition; **d** good bonding under good-weld condition; **e** over-weld (e.g. at $p = 4$ bar, $a = 55$ µm and $t = 0.60$ s) condition and **f** over-weld tab broken zone

were experienced partial circumferential fracture with adhesion with the Cu tabs. However, over-weld with full circumferential fracture resulted in material adhesion in the weld nugget with no material tear.

3.3 Microstructure-based weld quality

To reveal the microstructural joint characteristics of under-, good- and over-welds, representative samples (as indicated in Fig. 3) were cut, cold moulded and polished successively with SiC paper, diamond suspension solutions and colloidal silica solution. The microscopic inspection revealed the weld characteristics between the tabs and busbar and these weld characteristics were used for better understanding of the three weld categories. The main joining mechanisms reported in the literature are mechanical interlocking between the mating surfaces, local heating due to friction leading to diffusion across the interface and plastic deformation [1, 54]. A good-weld exhibits a strong adhesion of tabs to busbar without the presence of a gap at the interface which is the result of dense bonding [55]. Examples of under-weld, good-weld and over-weld conditions are shown in Fig. 13 where the optical cross-sectional images reveal the joint areas and their characteristics including bonded/un-bonded zone, tab-to-busbar gap, excessive tab material thinning and tab broken zone. Low magnification (× 5) based optical images were taken to capture the overall joint cross-sections whereas higher magnification (× 50) was used to capture the detailed bonding characteristics. In the under-weld condition, Al tabs were loosely bonded with the Cu busbar and higher magnification (× 50), as shown in Fig. 13(b), exhibits the intermittent un-bonded gap between tabs and busbar. The under-weld occurred due to lower values of process parameters which were not

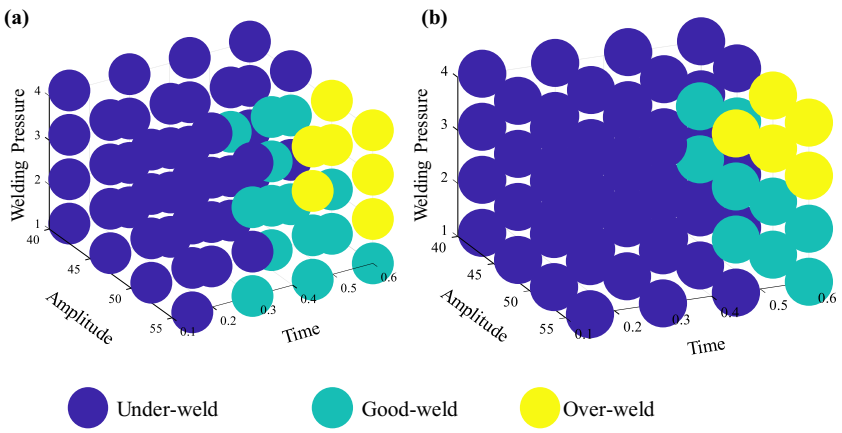

Fig. 14 Weldability zone for **a** lap shear, and **b** T-peel

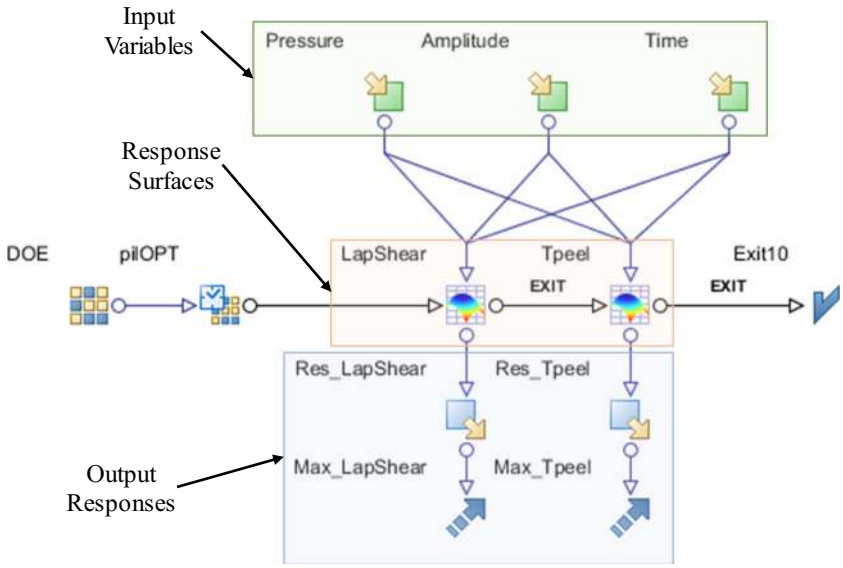

Fig. 15 Optimisation workflow in the modeFRONTIER® platform used for lap shear and T-peel strength maximisation

sufficient to create ultrasonic energy to break full oxide layers and ended with intermittent formation of microbonding [55]. For example, lower values of welding time and amplitude may not be able to create sufficient friction at the interface, and subsequently, resulted in inadequate heat generation to create atomic diffusion bonds across the mating surface [56]. Therefore, intermittent mechanical interlocking was the only joining mechanism which existed in under-weld and resulted in a weaker joint. However, further increase in process parameters resulted in higher friction, and subsequently, increased heat generation to produce uniform atomic diffusion bonds between tabs and busbar which was represented as good-weld [45]. Due to high bond density, high strength was obtained for good-weld condition. It is evident from the good-weld joint cross-section maps as shown in Fig. 13(c, d) that the tab-to-busbar joint interface has uniform bonding throughout the joint cross-section.

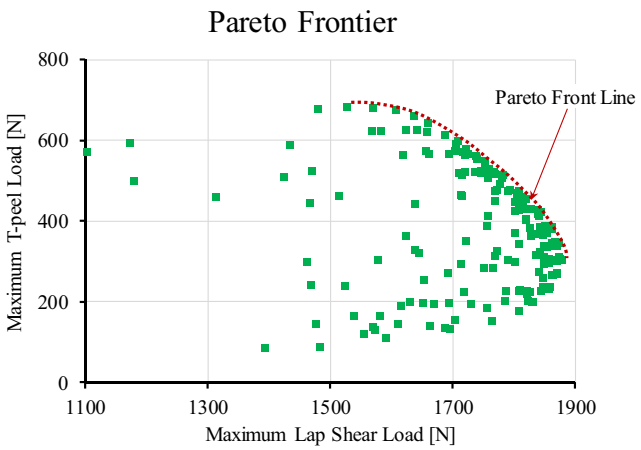

Fig. 16 Scatter plot showing the trade-off curve or Pareto Frontier obtained from maximum lap shear and T-peel loads

But, in case of over-weld, the Al tabs were heated extensively as they were exposed for longer time at higher amplitude and welding pressure. As a combined effect of higher values of process parameters, the aluminium became more ductile and heavily deformed which resulted in excessive thinning of tab materials. Often at higher values of process parameters, Cu busbar materials became visible from the top surface as the Al tab materials were extruded sidewise of the sonotrode. Figure 13(e, f) exhibits the tab thinning and tab broken zones which are exposing the Cu busbar. Furthermore, these excessive deformation and extrusion led to cracks in the Al tabs at its corners/edges which made the over-weld weaker than the good-weld.

3.4 Weld quality–based strength optimization

Good weldability region can be identified using the weld quality classification and response surface models for maximum lap shear and T-peel loads. For the first time, three-dimensional weldability zones have been defined using multi-layered ultrasonic welded Cu-Al joints. Figure 14 shows the scatter plots of weldability region for the under-weld, good-weld and over-weld quality using the results obtained from this study. Optimum ultrasonic metal welding process parameters have been established within the good-weld region for both maximum lap shear and T-peel loads. For the particular material/stack-up combination considered in this study, the good-weld region is bounded in between 1 and 2 bar welding pressures, 0.45–0.6 s welding time, and 45–55 μm amplitude. The relationship between the input process parameters (i.e. welding pressure, amplitude and welding time) on output variables (i.e. maximum lap shear and T-peel loads) were found in response surface models. Based on these response surface models coupled with obtained good

Table 5 Selected optimal design point with RSM-based and real confirmation experimental design evaluations

Selected optimal design point			Response variables					
Welding pressure [bar]	Amplitude [μm]	Welding time [s]	Lap shear load [N]			T-peel load [N]		
			RSM result	Confirmation experiments average	Error (%)	RSM result	Confirmation experiments average	Error (%)
1.1	55	0.55	1706.56	1659.46	2.7	601.74	651.42	7.6

weldability zone, optimum process parameters can be identified when objectives are to maximise both lap shear and T-peel strengths.

A multidisciplinary design optimization (MDO) platform, modeFRONTIER® was used for optimisation (https://www.esteco.com/modefrontier) which facilitates the process of integration of various design tables/tools and exchanging information among them [57] and it is one of the widely used for computational optimisation in UK engineering industries [58]. Basically, the response surface model–based optimisation is built in three stages: firstly, to develop effective meta-models/surrogate models based on the experimental/simulation trial results [59, 60]; secondly, to validate the meta-models using one or more algorithms to estimate the accuracy of each of the

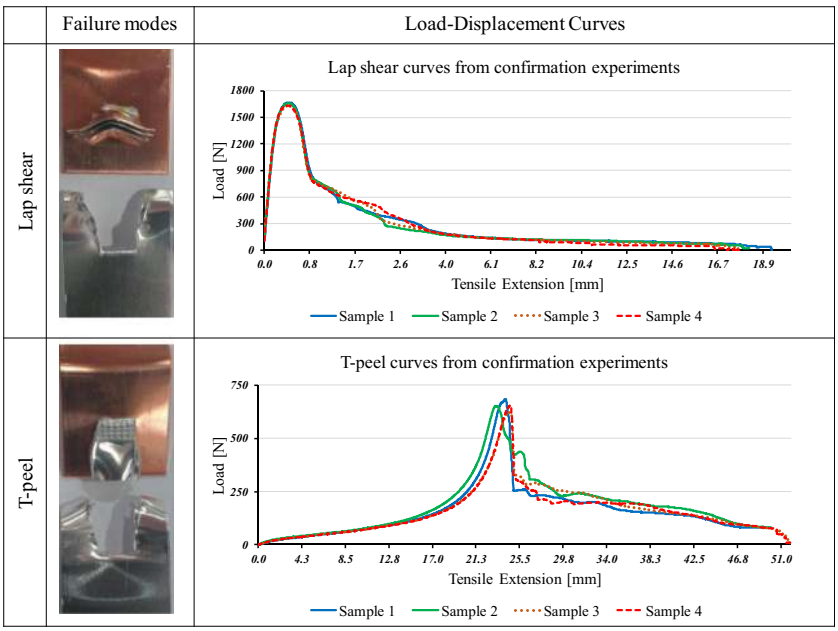

Fig. 17 Failure modes and load-displacement curves obtained from lap shear and T-peel confirmation tests

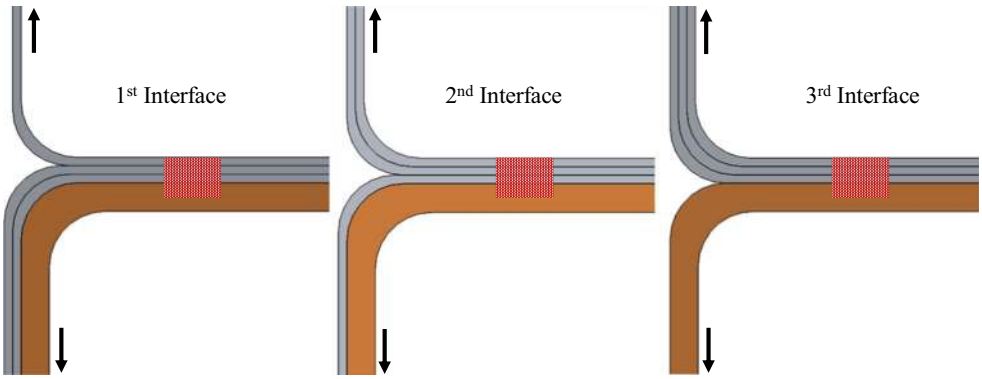

Fig. 18 Multi-layered joint weld interfaces for T-peel strength evaluation

models with insights feature [58]; and lastly, to use it to perform a virtual (RSM-based) optimisation [61, 62]. The optimisation workflow linking the input process parameters to output variables through developed response surface models is shown in Fig. 15. Multi-objective optimization algorithm–based pilOPT optimiser was used for this study due to several benefits such as multiple objectives, continuous input variables, and fast convergence with few evaluations. Furthermore, it is a hybrid multi-strategy self-adapting algorithm that combines the advantages of a local search and a global search algorithm and it adjusts the ratio of real and RSM-based design evaluations based on their performance (https://www.esteco.com/modefrontier) [63].

The optimisation was conducted based on the pilOPT optimiser considering two main objectives which were maximisation of lap shear and T-peel loads. The input process parameters were kept bounded in between the identified good weldability region. In general, it was observed that both lap shear and T-peel strength increased simultaneously until the lap shear load reached the maximum before decreasing with incremental increase in T-peel load. Therefore, a Pareto frontier was obtained, as shown in red dotted line in Fig. 16, which is basically a trade-off curve between the maximum lap shear and T-peel loads. For instance, the maximum lap shear load was at 1876 N and the corresponding T-peel load was 307.71 N or the maximum T-peel load was at 684.19 N with corresponding Lap sear load was 1526.90 N. Therefore, all the points on the Pareto front line are optimal solution and process designers have the flexibility to choose optimal design based on their design criteria and strength requirement. For example, when T-peel strength is more important than lap shear strength, the process designer can choose an optimal solution which yields higher T-peel load. In this study, an intermediate optimal point was selected for further study when the lap shear and T-peel loads are greater than 1700 N and 600 N, respectively. The selected optimal design point with input process parameters, respective RSM-based and real design evaluations are given in Table 5. Ultrasonic metal welding was conducted at the selected optimal design point and corresponding confirmation experimental results are reported for both lap shear and T-peel tests. Furthermore, load-displacement curves with failure modes obtained from lap shear and T-peel confirmation tests are given in Fig. 17. The obtained standard errors from the lap shear and T-peel confirmation tests are 9.7 and 13.07, respectively. It can be observed that RSM-based results are closely agreeing with confirmation experimental results. At the optimal design point, the lap shear was overestimated by 2.7% and T-peel strength was underestimated by 7.6%. These may be attributed to the regression equations used to explain the welding behaviour and the coefficient of determination for lap shear regression is higher than the T-peel regression.

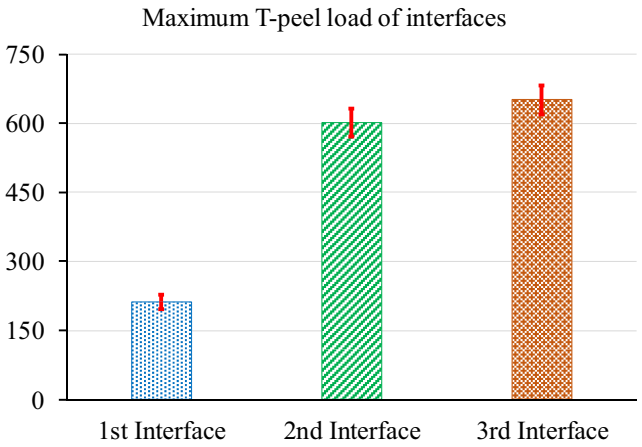

Fig. 19 T-peel test loads of multi-layered joint weld interfaces

3.5 T-peel strength of interfaces

Relying on the selected optimal design point, this paper further evaluates the T-peel strength of individual interfaces. Due to the multi-layered configuration, each weld has three interfaces as shown in Fig. 18. For evaluating strength of the interfaces, T-peel test is ideal as the interfaces can clearly be separated compared to lap shear test and specimens can be gripped by the pulling jaws. The same test conditions as described in Section 2.3 were applied for strength evaluation of the interfaces. In Fig. 19, maximum T-peel loads obtained from three different interfaces are reported. It can be seen that the 1st layer, 2nd layer and 3rd layer maximum T-peel loads are 212.74 N, 601.21 N and 651.42 N, respectively. The failure mode obtained from the T-peel tests of these three interfaces was partial interfacial separation with tear which was expected as optimal welding condition that also yielded the same failure mode as reported in Section 3.2. The first interface is actually representing the T-peel load of single Al tab which is expected to be lower than the second and third interfaces as they represent two or three Al tabs combined, respectively.

4 Conclusions

In this paper, a process robustness and shear strength analysis were conducted for ultrasonic metal welding considering multi-layered dissimilar materials. For this study, single layer of copper busbar to three layers of aluminium tabs are welded together to represent electric vehicle battery interconnects. The effects of input process parameters (i.e. welding pressure, amplitude and welding time) on lap shear and T-peel strengths were reported along with detailed analysis of failure modes. Full factorial design was chosen to conduct the experiments according to varying welding pressure, amplitude and welding

time. Based on the results obtained from this study, the following conclusions were drawn:

- The main effects and interactions of the input process parameters on the maximum lap shear and T-peel loads revealed that they had complex behaviour. It was found that third-order polynomial regression equations can sufficiently explain the maximum lap shear and T-peel loads. The response surfaces and corresponding contour plots showed that the ultrasonic metal welding process was sensitive to process variation which required systematic approach to optimise the process.
- The process variation was required to be classified in the three categories, i.e. under-weld, good-weld and over-weld to identify the best feasible weldability region. This paper identifies the good weldability region by combining the results from failure mode analysis and developed response surfaces.
- The optimisation was conducted within the identified good weldability region which gave a Pareto Frontier i.e. a trade-off between two objective functions. This indicated that all the design points on the Pareto front were optimal to maximise both lap sear and T-peel loads.
- Confirmation experiments were conducted to verify and validate the selection optimal lap shear and T-peel loads. Further, this optimal joint was used to evaluate the T-peel strength of individual interfaces.
- A systematic guideline was developed in this study to optimise ultrasonic welding process for automotive electric vehicle battery joining application. Further, the optimised welded joints can be used for electrical and thermal characterisation as future work.

Acknowledgements This research is partially supported by the WMG Centre High Value Manufacturing (HVM) Catapult at The University of Warwick.

References

1. Shakil M, Tariq NH, Ahmad M, Choudhary MA, Akhter JI, Babu SS (2014) Effect of ultrasonic welding parameters on microstructure and mechanical properties of dissimilar joints. Mater Des 55: 263–273. https://doi.org/10.1016/j.matdes.2013.09.074
2. Elangovan S, Prakasan K, Jaiganesh V (2010) Optimization of ultrasonic welding parameters for copper to copper joints using design of experiments. Int J Adv Manuf Technol 51(1):163–171. https://doi.org/10.1007/s00170-010-2627-1
3. Siddiq A, Ghassemieh E (2008) Thermomechanical analyses of ultrasonic welding process using thermal and acoustic softening effects. Mech Mater 40(12):982–1000. https://doi.org/10.1016/j.mechmat.2008.06.004
4. Kim TH, Yum J, Hu SJ, Spicer JP, Abell JA (2011) Process robustness of single lap ultrasonic welding of thin, dissimilar materials. CIRP Ann Manuf Technol 60(1):17–20. https://doi.org/10.1016/j.cirp.2011.03.016
5. Neppiras EA (1965) Ultrasonic welding of metals. Ultrasonics 3(3): 128–135. https://doi.org/10.1016/S0041-624X(65)80003-8
6. Bakavos D, Prangnell PB (2010) Mechanisms of joint and microstructure formation in high power ultrasonic spot welding 6111 aluminium automotive sheet. Mater Sci Eng A 527(23):6320–6334. https://doi.org/10.1016/j.msea.2010.06.038
7. Lee SS, Kim TH, Hu SJ, Cai WW, Abell JA (2010) Joining technologies for automotive lithium-ion battery manufacturing: a review. In: ASME 2010 International Manufacturing Science and Engineering Conference, Pennsylvania, USA, pp 541–549
8. Zhang CQ, Robson JD, Prangnell PB (2016) Dissimilar ultrasonic spot welding of aerospace aluminum alloy AA2139 to titanium alloy TiAl6V4. J Mater Process Technol 231:382–388. https://doi.org/10.1016/j.jmatprotec.2016.01.008
9. Ventrella VA, Berretta JR, de Rossi W (2010) Pulsed Nd:YAG laser seam welding of AISI 316L stainless steel thin foils. J Mater Process Technol 210(14):1838–1843. https://doi.org/10.1016/j.jmatprotec.2010.06.015
10. Hirata Y (2003) Pulsed arc welding. Weld Int 17(2):98–115. https://doi.org/10.1533/wint.2003.3075
11. Brand MJ, Schmidt PA, Zaeh MF, Jossen A (2015) Welding techniques for battery cells and resulting electrical contact resistances. J Energy Storage 1:7–14. https://doi.org/10.1016/j.est.2015.04.001
12. De Vries E (2004) Mechanics and mechanisms of ultrasonic metal welding. The Ohio State University
13. Das A, Li D, Williams D, Greenwood D (2018) Joining technologies for automotive battery systems manufacturing. World Electr Veh J 9(2):22. https://doi.org/10.3390/wevj9020022
14. Annoni M, Carboni M (2011) Ultrasonic metal welding of AA 6022-T4 lap joints: part I – technological characterisation and static mechanical behaviour. Sci Technol Weld Join 16(2):107–115. https://doi.org/10.1179/1362171810Y.0000000014
15. Matsuoka S-i, Imai H (2009) Direct welding of different metals used ultrasonic vibration. J Mater Process Technol 209(2):954–960. https://doi.org/10.1016/j.jmatprotec.2008.03.006
16. Matsuoka S-i (1994) Ultrasonic welding of ceramic/metal. J Mater Process Technol 47(1):185–196. https://doi.org/10.1016/0924-0136(94)90094-9
17. Dinda SK, Basiruddin Sk M, Roy GG, Srirangam P (2016) Microstructure and mechanical properties of electron beam welded dissimilar steel to Fe–Al alloy joints. Mater Sci Eng A 677:182–192. https://doi.org/10.1016/j.msea.2016.09.050
18. Russo Spena P, De Maddis M, Lombardi F, Rossini M (2016) Dissimilar resistance spot welding of Q&P and TWIP steel sheets. Mater Manuf Process 31(3):291–299. https://doi.org/10.1080/10426914.2015.1048476
19. Mai TA, Spowage AC (2004) Characterisation of dissimilar joints in laser welding of steel–kovar, copper–steel and copper–aluminium. Mater Sci Eng A 374(1):224–233. https://doi.org/10.1016/j.msea.2004.02.025
20. Das A, Butterworth I, Masters I, Williams D (2018) Microstructure and mechanical properties of gap-bridged remote laser welded (RLW) automotive grade AA 5182 joints. Mater Charact 145: 697–712. https://doi.org/10.1016/j.matchar.2018.09.035

21. Briskham P, Blundell N, Han L, Hewitt R, Young K, Boomer D (2006) Comparison of self-pierce riveting, resistance spot welding and spot friction joining for aluminium automotive sheet. **SAE Technical Paper**,
22. Li D, Chrysanthou A, Patel I, Williams G (2017) Self-piercing riveting-a review. Int J Adv Manuf Technol 92(5–8):1777–1824
23. Guo JF, Chen HC, Sun CN, Bi G, Sun Z, Wei J (2014) Friction stir welding of dissimilar materials between AA6061 and AA7075 Al alloys effects of process parameters. Mater Des 56:185–192. https://doi.org/10.1016/j.matdes.2013.10.082
24. Uzun H, Dalle Donne C, Argagnotto A, Ghidini T, Gambaro C (2005) Friction stir welding of dissimilar Al 6013-T4 to X5CrNi18-10 stainless steel. Mater Des 26(1):41–46. https://doi.org/10.1016/j.matdes.2004.04.002
25. Faria R, Moura P, Delgado J, de Almeida AT (2012) A sustainability assessment of electric vehicles as a personal mobility system. Energy Convers Manag 61:19–30. https://doi.org/10.1016/j.enconman.2012.02.023
26. Whittingham MS (2012) History, evolution, and future status of energy storage. Proc IEEE 100:0018–9219
27. Shawn Lee S, Hyung Kim T, Jack Hu S, Cai WW, Abell JA, Li J (2013) Characterization of joint quality in ultrasonic welding of battery tabs. J Manuf Sci Eng 135 (2):021004–021004–021013. doi:https://doi.org/10.1115/1.4023364
28. Kong CY, Soar RC, Dickens PM (2005) A model for weld strength in ultrasonically consolidated components. Proc Inst Mech Eng C J Mech Eng Sci 219(1):83–91. https://doi.org/10.1243/095440605X8315
29. Macwan A, Patel VK, Jiang XQ, Li C, Bhole SD, Chen DL (2014) Ultrasonic spot welding of Al/Mg/Al tri-layered clad sheets. Mater Des 62:344–351. https://doi.org/10.1016/j.matdes.2014.05.035
30. Ni ZL, Ye FX (2016) Dissimilar joining of aluminum to copper using ultrasonic welding. Mater Manuf Process 31(16):2091–2100. https://doi.org/10.1080/10426914.2016.1221101
31. Yang J, Cao B, He X, Luo H (2014) Microstructure evolution and mechanical properties of Cu–Al joints by ultrasonic welding. Sci Technol Weld Join 19(6):500–504
32. Haddadi F, Abu-Farha F (2016) The effect of interface reaction on vibration evolution and performance of aluminium to steel high power ultrasonic spot joints. Mater Des 89:50–57. https://doi.org/10.1016/j.matdes.2015.09.121
33. Patel VK, Bhole SD, Chen DL (2012) Microstructure and mechanical properties of dissimilar welded Mg–Al joints by ultrasonic spot welding technique. Sci Technol Weld Join 17(3):202–206. https://doi.org/10.1179/1362171811Y.0000000094
34. Wang SQ, Patel VK, Bhole SD, Wen GD, Chen DL (2015) Microstructure and mechanical properties of ultrasonic spot welded Al/Ti alloy joints. Mater Des 78:33–41. https://doi.org/10.1016/j.matdes.2015.04.023
35. Macwan A, Chen DL (2015) Microstructure and mechanical properties of ultrasonic spot welded copper-to-magnesium alloy joints. Mater Des 84:261–269. https://doi.org/10.1016/j.matdes.2015.06.104
36. Janaki Ram GD, Yang Y, Stucker BE (2006) Effect of process parameters on bond formation during ultrasonic consolidation of aluminum alloy 3003. J Manuf Syst 25(3):221–238. https://doi.org/10.1016/S0278-6125(07)80011-2
37. Kang B, Cai W, Tan C-A (2014) Vibrational energy loss analysis in battery tab ultrasonic welding. J Manuf Process 16(2):218–232. https://doi.org/10.1016/j.jmapro.2013.10.008
38. Kang B, Cai W, Tan C-A (2014) Dynamic stress analysis of battery tabs under ultrasonic welding. J Manuf Sci Eng 136(4):041011–041011. https://doi.org/10.1115/1.4026990
39. Lee D, Kannatey-Asibu E, Cai W (2013) Ultrasonic welding simulations for multiple layers of lithium-ion battery tabs. J Manuf Sci Eng 135 (6):061011–061011–061013. doi:https://doi.org/10.1115/1.4025668
40. Shawn Lee S, Hyung Kim T, Jack Hu S, Cai WW, Abell JA (2015) Analysis of weld formation in multilayer ultrasonic metal welding using high-speed images. J Manuf Sci Eng 137 (3):031016–031016–031018. doi:https://doi.org/10.1115/1.4029787
41. Design Possibilities for the Chevy Bolt (2015) http://gm-volt.com/2015/06/19/design-possibilities-for-the-chevy-bolt/. Accessed 2017-07-05
42. Cai W, Blau PJ, Qu J (2013) Friction coefficients of battery metals and the usage in ultrasonic welding simulations. In: 2013 World Electric Vehicle Symposium and Exhibition (EVS27), 17-20 Nov. 2013, pp 1–10. https://doi.org/10.1109/EVS.2013.6914778
43. Elangovan S, Semeer S, Prakasan K (2009) Temperature and stress distribution in ultrasonic metal welding—an FEA-based study. J Mater Process Technol 209(3):1143–1150. https://doi.org/10.1016/j.jmatprotec.2008.03.032
44. Zhang C, Li L (2009) A coupled thermal-mechanical analysis of ultrasonic bonding mechanism. Metall Mater Trans B 40(2):196–207. https://doi.org/10.1007/s11663-008-9224-9
45. Gunduz IE, Ando T, Shattuck E, Wong PY, Doumanidis CC (2005) Enhanced diffusion and phase transformations during ultrasonic welding of zinc and aluminum. Scr Mater 52(9):939–943. https://doi.org/10.1016/j.scriptamat.2004.12.015
46. Kreye H. Melting phenomena in solid state welding processes
47. Harthoorn J (1978) Ultrasonic metal welding. Technische Hogeschool Eindhoven
48. Li J, Han L, Zhong J (2008) Short-circuit diffusion of ultrasonic bonding interfaces in microelectronic packaging. 40 (5):953–957. https://doi.org/10.1002/sia.2840
49. Montgomery DC (2017) Design and analysis of experiments. **John wiley & sons**,
50. Rakić T, Kasagić-Vujanović I, Jovanović M, Jančić-Stojanović B, Ivanović D (2014) Comparison of full factorial design, central composite design, and box-Behnken design in chromatographic method development for the determination of fluconazole and its impurities. Anal Lett 47(8):1334–1347. https://doi.org/10.1080/00032719.2013.867503
51. Myers RH, Montgomery DC, Anderson-Cook CM (2009) Response surface methodology: process and product optimization using designed experiments, vol 705. John Wiley & Sons,
52. Alfeld P (1989) Scattered data interpolation in three or more variables A2 - LYCHE, TOM. In: Schumaker LL (ed) Mathematical methods in computer aided geometric design. Academic Press, pp 1–33. https://doi.org/10.1016/B978-0-12-460515-2.50005-6
53. Fujita K, Kounoe Y (2006) High-order polynomial response surface with optimal selection of interaction terms. In: 11th AIAA/ISSMO Multidisciplinary Analysis and Optimization Conference. Multidisciplinary Analysis Optimization Conferences. American Institute of Aeronautics and Astronautics. https://doi.org/10.2514/6.2006-7054
54. Gencsoy H, Adams J, Shin SJU (1967) On some fundamental problems in ultrasonic welding of dissimilar metals. Weld J 46(4): 145-s 5 (4):274
55. Satpathy MP, Moharana BR, Dewangan S, Sahoo SK (2015) Modeling and optimization of ultrasonic metal welding on dissimilar sheets using fuzzy based genetic algorithm approach. Eng Sci Technol Int J 18(4):634–647. https://doi.org/10.1016/j.jestch.2015.04.007
56. Satpathy MP, Sahoo SK (2017) Mechanical performance and metallurgical characterization of ultrasonically welded dissimilar joints. J Manuf Process 25:443–451. https://doi.org/10.1016/j.jmapro.2017.01.001
57. Safavi E, Tarkian M, Gavel H, Ölvander J (2015) Collaborative multidisciplinary design optimization: a framework applied on

aircraft conceptual system design. Concurr Eng 23(3):236–249. https://doi.org/10.1177/1063293X15587020

58. Tiwari A, Hoyos PN, Hutabarat W, Turner C, Ince N, Gan X-P, Prajapat N (2015) Survey on the use of computational optimisation in UK engineering companies. CIRP J Manuf Sci Technol 9:57–68. https://doi.org/10.1016/j.cirpj.2015.01.003
59. Das A, Franciosa P, Pesce A, Gerbino S (2017) Parametric effect analysis of free-form shape error during sheet metal forming. Int J Eng Sci Technol 9(09S):117–124
60. Das A, Franciosa P, Gerbino S, Williams D (2016) Prediction of geometric errors of stamped sheet metal parts using deviation field decomposition. In: International conference on competitive manufacturing (COMA), Stellenbosch, South Africa, pp 109–114
61. Shi X (2011) Design optimization of insulation usage and space conditioning load using energy simulation and genetic algorithm. Energy 36(3):1659–1667. https://doi.org/10.1016/j.energy.2010.12.064
62. Das A, Franciosa P, Ceglarek D (2015) Fixture design optimisation considering production batch of compliant non-ideal sheet metal parts. Procedia Manuf 1:157–168. https://doi.org/10.1016/j.promfg.2015.09.079
63. Cicconi P, Germani M, Bondi S, Zuliani A, Cagnacci E (2016) A design methodology to support the optimization of steel structures. Procedia CIRP 50:58–64. https://doi.org/10.1016/j.procir.2016.05.030